Broadband angle-independent antireflection coatings on nanostructured light trapping solar cells

Abraham Vázquez-Guardado,[1,2] Javaneh Boroumand,[2,3] Daniel Franklin,[2,3] and Debashis Chanda[1,2,3,*]
[1]CREOL, College of Optics and Photonics, University of Central Florida, Orlando, Florida 32816, USA
[2]NanoScience Technology Center, University of Central Florida, Orlando, Florida 32826, USA
[3]Department of Physics, University of Central Florida, Orlando, Florida 32816, USA

(Received 13 November 2017; revised manuscript received 13 January 2018; published 22 March 2018)

Backscattering from nanostructured surfaces greatly diminishes the efficacy of light trapping solar cells. While the analytical design of broadband, angle-independent antireflection coatings on nanostructured surfaces proved inefficient, numerical optimization proves a viable alternative. Here, we numerically design and experimentally verify the performance of single and bilayer antireflection coatings on a 2D hexagonal diffractive light trapping pattern on crystalline silicon substrates. Three well-known antireflection coatings, aluminum oxide, silicon nitride, and silicon oxide, which also double as high-quality surface passivation materials, are studied in the 400–1000 nm band. By varying thickness and conformity, the optimal parameters that minimize the broadband total reflectance (specular and scattering) from the nanostructured surface are obtained. The design results in a single-layer antireflection coating with normal-angle wavelength-integrated reflectance below 4% and a bilayer antireflection coating demonstrating reflection down to 1.5%. We show experimentally an angle-averaged reflectance of ∼5.2% up to 60° incident angle from the optimized bilayer antireflection-coated nanostructured surface, paving the path toward practical implementation of the light trapping solar cells.

DOI: 10.1103/PhysRevMaterials.2.035201

I. INTRODUCTION

The performance of many optoelectronic devices, such as photodetectors and solar cells, relies intrinsically on the efficient absorption of light. Apart from enhancing the absorption within the bulk of the semiconductor, there are studies on antireflection coating materials [1–5], their deposition methods [6,7], and nano/microstructured antireflection coatings (ARC) [8–18] in which the focus is to minimize reflection losses and increase transmission into semiconductor substrate. Therefore, further maximizing the bulk semiconductor absorption with techniques that simultaneously reduce reflection and increase transmission continues to be of great scientific and commercial interest.

The most common ARC is a single dielectric layer, usually a quarter-wave configuration on a flat interface, that serves to bridge the optical impedance of free space and the generally high-index semiconductor—for a specific wavelength. Although, such dielectric-based ARCs are shown to minimize the integrated reflectivity down to $< 2\%$ [11,19], they do not necessarily maximize the photon absorption in the substrate. For instance, silicon thinner than 150 μm is unable to absorb the full solar spectrum within one optical pass and the unabsorbed light partially transmits out of the cell. In order to increase light absorption in such thin semiconductor slabs, deterministic light trapping (LT) patterns, which efficiently diffract incoming radiation toward the semiconductor, have been previously demonstrated [12,14,20–34]. However, in order to benefit from both ARCs and LT schemes and enhance overall light absorption within thin solar cells, a unified light trapping and antireflection scheme is of paramount importance. Cells nanostructured with two-dimensional diffraction gratings have demonstrated enhanced absorption by increasing the effective path length of light within the absorbing medium [24,31,35]. In our earlier works, we have demonstrated significant wavelength-integrated absorption enhancement up to about ∼200% in ultrathin *c*-Si films (3–6 μm) based on a two-dimensional (2D) hexagonal array of posts [24,30,31]. However, a broadband angle-independent ARC, which can further reduce the reflection loss from the nanostructured front surface, remains as a challenge. In contrast with other structures such as black silicon [36,37] or various photonic crystals [38,39], the proposed ARC-LT scheme presented here not only allows broadband reflectance minimization over broad angle of incidences but enhances absorption [24,31,35]. It also reduces surface recombination losses by keeping the total surface area lower compared to micropyramid random texturing [22,40–43] or black-silicon [36,37,44].

In this work, we report the design and optimization of antireflection coatings on an optimized 2D LT nanostructure [24,31]. The main goal is to reduce the total reflection loss by numerically minimizing the averaged total reflectance with respect to the solar irradiance (AM1.5) over a broad wavelength band (400–1100 nm) as a function of dielectric ARCs. In contrast with previously reported LT-ARC [14], the present work differs in three major aspects: (1) Unlike the referred work where only Si_3N_4 is studied as an ARC material, the present work went further and studied Si_3N_4, SiO_2, and Al_2O_3 as a common ARC and surface passivation layers, (2) proposed and demonstrated a bilayer ARC film to further reduce wavelength-integrated reflection <2% from the nanostructured surface, and (3) studied the effect of conformal coating thickness variation. This is very important as in reality chemical vapor deposition

*debashis.chanda@creol.ucf.edu

 ©2018 American Physical Society

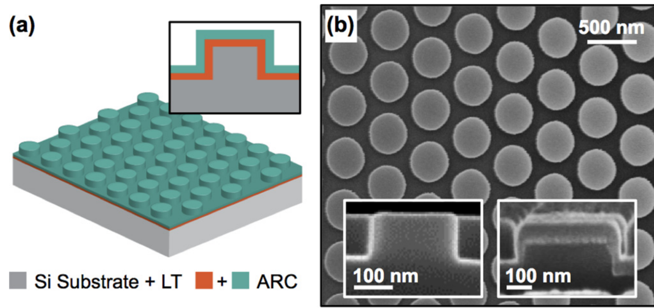

FIG. 1. Device schematic and SEM. (a) Device schematic of the light trapping pattern with antireflective coating. (b) Top-view SEM image of one fabricated LT sample with cross section in the left inset. Left and right insets show the cross section SEM of two LT devices without and with ARC, respectively.

(CVD)-grown ARC layer thickness varies across a patterned surface unlike a uniform surface. The optimized ARC layer on this nanostructured surface reduces reflection loss and further enhances transmittance into the silicon substrate, improving total light absorption. We employed metal-assisted chemical etching (MacEtch) to pattern the light trapping nanostructure on the silicon surface [45], which serves as a low-cost alternative to reactive ion etching while maintaining control over structural features and simultaneously producing smooth surfaces needed for high-quality passivation [46]. Lastly, we experimentally demonstrate the combined, optimized ARC-LT system's wide-angle response, needed for high-efficiency solar cells.

II. RESULTS AND DISCUSSION

In this study we employ our previously optimized 2D diffractive grating that consists of a hexagonal array of posts on a crystalline silicon substrate with period = 500 nm, diameter = 300 nm, and height = 140 nm [24,31]. A schematic of the *c*-Si substrate with ARC-LT layers is shown in Fig. 1(a). The light trapping patterned silicon substrate is fabricated using the soft nanoimprint technique followed by MacEtch (see Methods for more details). The corresponding top and cross-sectional scanning electron microscopy (SEM) images of the bare and ARC coated light trapping patterns are shown in Fig. 1(b).

The proposed combined LT-ARC proves useful as neither the purely diffractive LT nor the simple ARC can provide a broadband reduction in reflectance. On one hand, it functions as an effective medium for wavelengths longer than ∼500 nm (cutoff ∼period) and consequently reduces the impedance mismatch increasing the transmission into the silicon substrate. At shorter wavelengths the LT pattern diffracts light that increases the backscattering as observed in reflection spectrum. On the other hand, in transmission it allows diffraction for any wavelength shorter that 1.75 μm (cutoff ∼index*period). This way transmitted light fans out, providing multiple propagation paths covering the silicon absorption band (400–1100 nm) enhancing the material absorption probability as previously demonstrated [24,31,35]. Overall, the composite LT+ARC film reduces reflection as well as increases absorption of light over a broad spectral and angular range. Furthermore, in LT-ARC systems, an increase in the surface area increases the total surface recombination losses, which is detrimental for solar cells' performance, as we have previously studied [31]. Therefore, it is important to keep the area enhancement factor as low as possible while exploiting reduced reflectance [22,44]. The proposed shallow 120–140-nm-deep diffractive pattern increases 1.6 times the surface area, which is much lower compared to ∼2.7 times in the microscale pyramidal texturing in conventional solar cells [11,17,40–43] or ∼5.2 in black silicon [36,37,44].

In conventional ARC configurations, the reflection from a flat surface (n_s) in free space ($n_{\mathrm{air}} = 1$) is minimized with a single-layer ARC (n_{ARC}) when its optical path length is a quarter wavelength of light, $d = \lambda/4n_{\mathrm{ARC}}$, where d is the ARC film thickness and with the condition that $n_s > n_{\mathrm{ARC}} > n_{\mathrm{air}}$. Reflection can even become zero if the refractive index of the ARC layer satisfies $n_{\mathrm{ARC}} = \sqrt{n_{\mathrm{air}} n_s}$ [47]. Nevertheless, such a condition fulfills only at a particular wavelength and angle of incidence on a flat interface, which is not the working condition and configuration in solar cell applications. In contrast, broadband ARC design on a nanostructured surface does not follow a straightforward analytical phase calculation due to its diffractive nature; instead, full-vectorial 3D numerical simulations are a better and more accurate alternative solution. Furthermore, for solar cells applications ARC materials must also provide a high-quality surface passivation to ensure minimal charge-carrier loss, which restricts to aluminum oxide (Al_2O_3), silicon nitride (Si_3N_4), and silicon dioxide (SiO_2) as the three most suitable ARC materials.

The unified LT-ARC system is numerically modeled using the finite difference time domain (FDTD) method to obtain the reflectance spectrum $R(\lambda)$ covering from 400 to 1100 nm (see Methods for more details). The integrated reflectance spectra weighted with the solar spectral irradiance $S(\lambda)$ (AM1.5) is used to determine the reflectance loss efficacy of the corresponding LT-ARC configuration, given by

$$\tilde{R} = \frac{\int R(\lambda)S(\lambda)d\lambda}{\int S(\lambda)d\lambda}. \quad (1)$$

A single-layer ARC, whose thickness is varied from 10 to 160 nm, conformally coats the LT structure. Figure 2(a) shows the reflectance dispersion spectra for SiO_2 ($n_{\mathrm{SiO}} = 1.47$), Si_3N_4 ($n_{\mathrm{SiN}} = 2$), and Al_2O_3 ($n_{\mathrm{AlO}} = 1.67$) ARC film, respectively. The results from these simulations [dashed line in Fig. 2(a)] demonstrate that minimum wavelength-integrated reflectance is obtained at a certain film thickness: 3.4% at 80 nm for SiO_2, 3.2% at 50 nm for Si_3N_4, and 3.2% at 60 nm for Al_2O_3. The reflectance spectra at these optimum ARC thicknesses are plotted in Fig. 2(b) alongside the reflection from flat and LT patterned silicon substrates without ARC for comparison. From this plot, it can be observed that the LT pattern alone reduces reflection significantly over the visible spectral range from average 34.6 to 8.1%. However, in the near-IR wavelength range (800–1100 nm), the LT pattern incurs high reflection loss (∼10%), which is much larger than that of the ARC-coated LT pattern ($< 3.5\%$). The wavelength-integrated reflectance for thicknesses of 10–160 nm are shown in Fig. 2(c) for all three ARCs on flat (dashed lines) and LT patterned silicon (solid lines). According to these predictions,

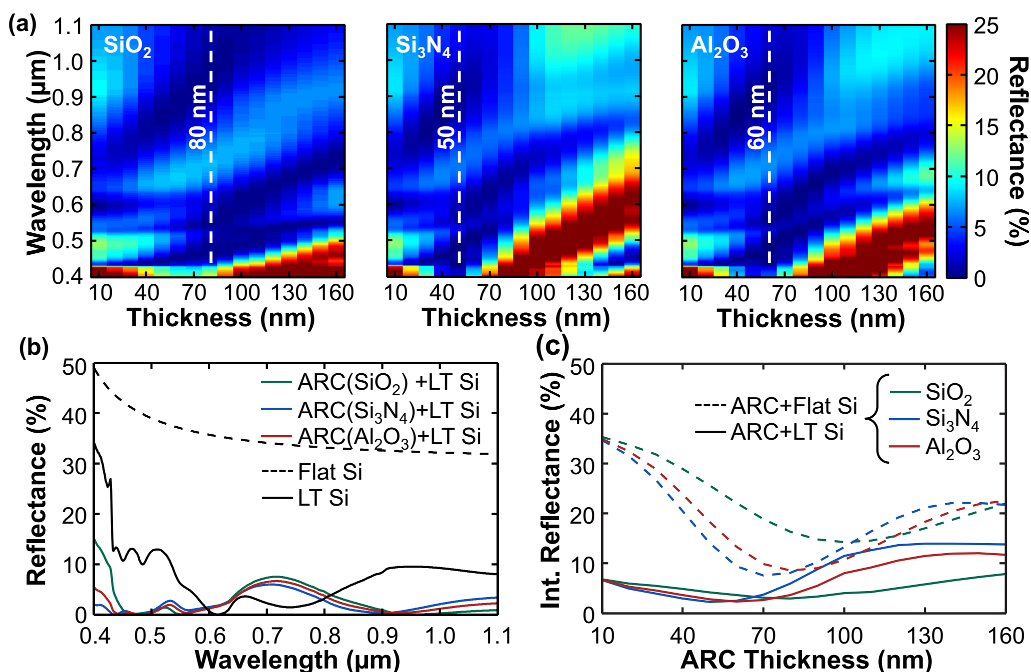

FIG. 2. Single-layer ARC optimization and optical characterization. (a) Reflectance as a function of wavelength and thickness for three single-layer ARCs, SiO_2 (left), Si_3N_4 (center), and Al_2O_3 (right) for a defined LT nanostructure. White lines indicate the thickness that gives the minimum wavelength-integrated reflectance. (b) Reflectance comparison of flat silicon (dashed line), LT patterned silicon (black solid line), and LT patterned Si coated with SiO_2 (green), Si_3N_4 (blue), and Al_2O_3 (red), for the corresponding optimized thickness indicated by the white dashed lines in (a). (c) Wavelength-integrated reflectance as a function of ARC thicknesses for flat (dashed) and LT patterned silicon (solid).

the minimum wavelength-integrated reflectance from a single-layer SiO_2, Si_3N_4, and Al_2O_3 on a flat silicon substrate [dashed lines in Fig. 2(c)] is obtained at 100, 70, and 80 nm, compared to 80, 50, and 60 nm for optimized LT-ARC, respectively. The optimized ARC-coated LT pattern [solid lines in Fig. 2(c)] corresponds to total integrated reflectance reduction of 78, 69, and 71%, respectively, with respect to the minimum reflectance obtained from the flat silicon with optimized ARC.

In the above numerical studies, all ARC coatings are considered to be conformal, i.e., having a uniform thickness across the nanostructured surface. However, in reality, a number of factors impact the uniformity of ARC such as deposition methods [plasma-enhanced chemical-vapor deposition (PECVD), low-pressure chemical vapor deposition (LPCVD), atomic layer deposition (ALD), etc.)], temperature, gas environment, deposition rate, and the underlying nanostructure dimensions and aspect ratio [48]. Due to the thin-film effect on the nanostructured surface, the thickness variation or the step coverage of the ARC layer have direct impacts on the reflection property of the surface. Step coverage (*stepcover*) is defined by the ratio of a deposited film thickness on the sidewall (s) over the thickness on the top/bottom surface (t) as shown schematically in inset of Fig. 3. To investigate the impact of step coverage on the reflectivity, and therefore performance of the ARC coating, the numerical simulations are compared with experimental measurements. Wavelength-dependent reflectance is numerically calculated for all three ARC materials at their optimum thicknesses for three step coverages: conformal (100%), intermediate (60%), and low (20%) as shown in Fig. 3. The architecture here presented is a complex system where diffraction contributions from the light trapping pattern and the antireflection coating interact simultaneously. When the conformity decreases, with a limit at zero sidewall coating, the total system tends to be three diffraction gratings: the LT structure (the strongest one), a disk sitting on the pillars, and a continuous film at the bottom of the LT structure. As the sidewall coating thickness goes down, the mode index of the optical mode reduces, which makes the resonance blue shift along 2–5% reduction in the reflectance as observed in Fig. 3. This indicates that for better ARC performance, a lower sidewall coating is desired, but not always feasible with conventional deposition methods. From experimental characterization, we find the typical step-coverage values for PECVD SiO_2 and Si_3N_4 at 300 °C and ALD Al_2O_3 at 200 °C are 20, 60, and 80%, respectively. Using these values, we simulate the ARC-LT silicon substrate and retrieve the wavelength-integrated reflectance as a function of thickness to obtain their respective optimal ARC thicknesses as shown in Fig. 4(a).

Finally, the optimized experimental ARC-LT samples, i.e., step coverage and ARC thickness [dots in Fig. 4(a)], are numerically simulated. Figure 4(b) shows the experimental measurements for these optimized ARCs and the corresponding numerically simulated reflectance spectra with highly accurate predictions. Minor mismatches between experiment and numerical results are due to the slight differences in refractive index and estimated dimensions used in the numerical modeling.

In order to further reduce the reflection loss, a bilayer ARC is studied. The optimal conditions that minimize reflection for flat double-layer ARC at normal angle of incidence are

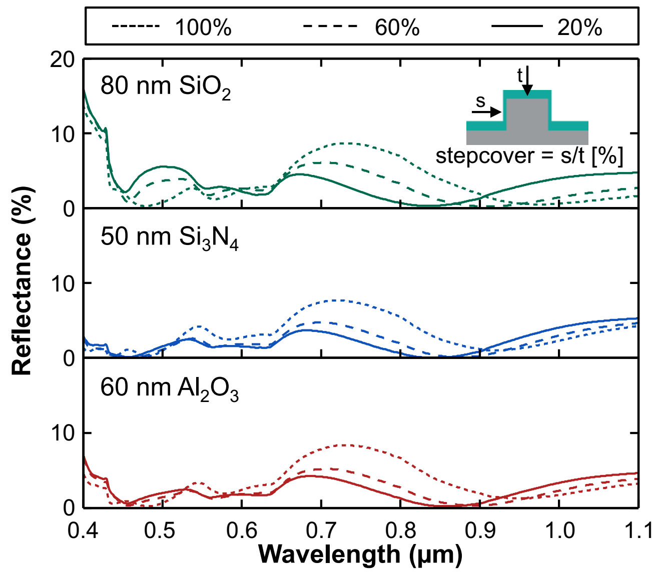

FIG. 3. Impact of step coverage on ARC performance. Comparison of the reflectance of the optimized SiO_2 (green), Si_3N_4 (blue), and Al_2O_3 (red) ARCs on LT patterned silicon substrate for three representative step coverage: 20% (solid lines), 60% (dashed lines), and 100% (dotted lines).

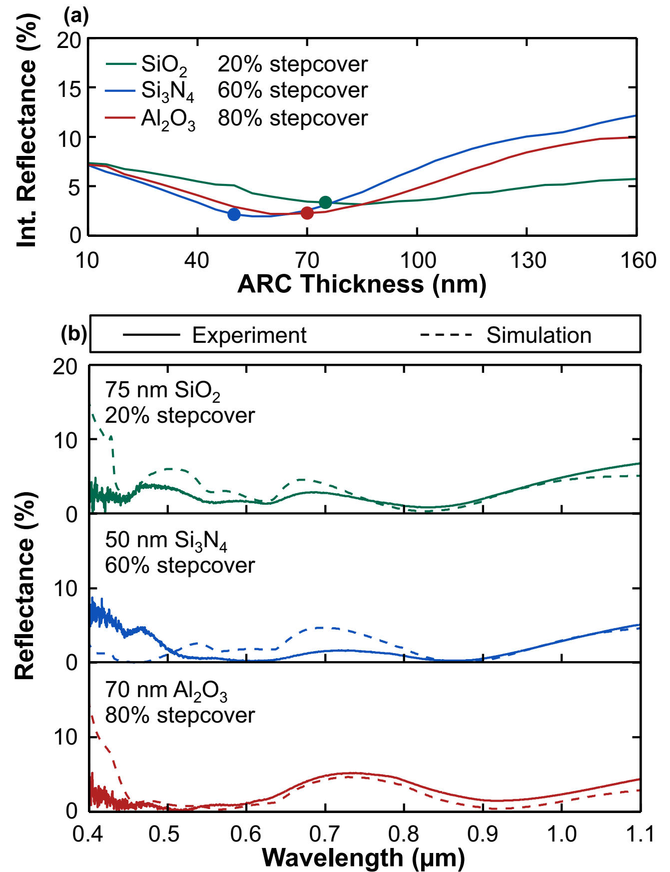

FIG. 4. Experimental verification and numerically predicted reflectance spectra. (a) Wavelength-integrated reflectance of each ARC with the corresponding step coverage determined by the deposition method: 20% for PECVD SiO_2 (green), 60% for PECVD Si_3N_4 (blue), and 80% for ALD Al_2O_3 (red). (b) Comparison of experimentally measured (continuous line) and numerically simulated (dotted line) ARC-LT silicon substrate for three optimized ARC thicknesses with its corresponding step coverage, dots in (a): 75 nm SiO_2 (green), 50 nm Si_3N_4 (blue), and 70 nm Al_2O_3 (red).

given by $n_1d_1 = n_2d_2 = \lambda/4$ [47], where $n_1/n_2 = \sqrt{n_{\mathrm{air}}/n_s}$, n_1 and n_2 are the refractive indices of the films in contact with air and silicon substrate, respectively. For a Si_3N_4 and SiO_2 bilayer, this corresponds to thicknesses of 70 and 90 nm, respectively, for flat silicon surface. Both silicon nitride and silicon oxide can be deposited in a PECVD system at the same temperature (300 °C), which keeps the fabrication process cost effective. To obtain a broadband and angle-independent response, we perform FDTD-based reflection minimization varying these two layers' thicknesses from 10 to 100 nm, for conformal and nonconformal cases, to predict the optimum thicknesses of each layer for the bilayer ARC on the light trapping nanostructure as shown in Fig. 5(a). According to these numerical predictions, for conformal ARC layers, the integrated reflectance gives a minimum reflectance of 2.4% at 30 nm Si_3N_4 and 70 nm SiO_2, indicated as a white dot. In the realistic nonconformal scenario, corresponding to our experimental fabrication (60% Si_3N_4-20% SiO_2), the minimum wavelength-integrated reflectance of ∼1.5% is obtained in the range of 60–70 nm Si_3N_4 and 100-nm SiO_2 over a broadband wavelength regime (400–1100 nm) as can be observed in Fig. 5(b). The lower reflectance value of the nonconformal case is due to the better performance of lower step coverage on the top diffractive pattern that was shown in Fig. 3. In order to experimentally verify this prediction, the reflectance versus wavelength of an ARC-LT patterned silicon coated with the optimized thickness of 70 nm Si_3N_4 at 60% step coverage and 100 nm SiO_2 at 20% step coverage is fabricated and measured as shown in Fig. 5(b). Good spectral agreement is observed between simulation and experimental results with integrated reflectance of 1.5 and 2.9%, respectively.

Finally, to quantify how this optimized ARC performs in the real solar cell context where sun moves across the sky, the combined wavelength and angular response of the system is studied. The FDTD predicted wavelength-integrated reflectivity as a function of incident angle is shown in Fig. 5(c). It is observed that the wavelength-integrated reflectance remains below 5% from 0–60° over the visible regime (400–850 nm). Not only is the bilayer ARC performing better than a single layer ARC in terms of low reflectivity, but its overall angle dependency is 53% lower than its optimized single-layer ARC components (Si_3N_4 or SiO_2). We then experimentally verify these simulations by using an integrating sphere (see Methods for more details). We observed an increment in reflectance from ∼2.5 to 4% for change in the incident angle from 0 to 10° [see Fig. 5(c)], contrary to the FDTD simulation which predicts a constant wavelength-integrated reflectance, possibly due to the inaccuracies of angle-dependent spectral measurements during the integrating sphere characterization. At normal incidence (i.e., 0°), SiO_2 and Si_3N_4 showed the same level of the measured integrated reflectance in Fig. 5(c), which is within <1% prediction accuracy of Fig. 4(a). For this complex multi-layer nanostructured surface, this is well within the acceptable norms. The measured angle-dependent wavelength-integrated

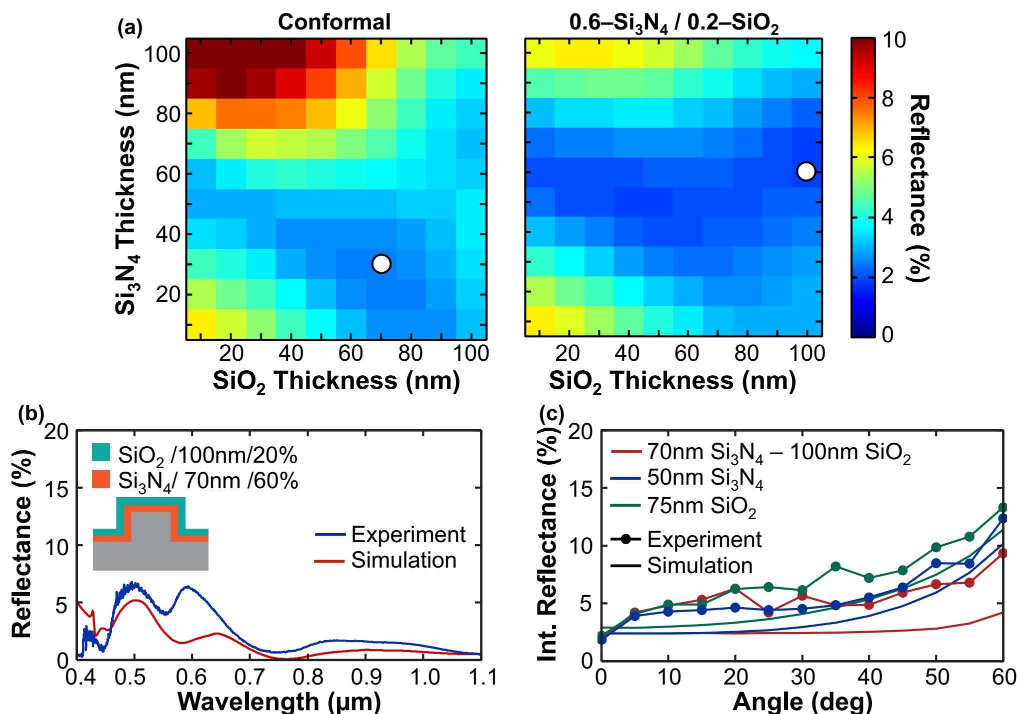

FIG. 5. Bilayer ARC thickness optimization and angular performance. (a) Numerically predicted wavelength-integrated reflectance as a function of Si_3N_4-SiO_2 bilayer ARC thickness for conformal (left) and nonconformal (right) coatings on LT-patterned silicon. The optimum ARC thicknesses at which the minimum wavelength-integrated reflection is obtained are marked as a white circle. (b) Experimentally measured and predicted reflectance spectra for nonconformal 70 nm Si_3N_4 at 20% step coverage and 100 nm SiO_2 at 60% step coverage bilayer ARC on LT patterned silicon substrate. (c) Numerically predicted (continuous line) and experimentally measured (dotted line) angle-dependent wavelength-integrated reflectance from the optimized ARC-coated LT patterned silicon.

reflectance for the optimized bilayer ARC-coated LT patterned silicon surface shows a better performance in comparison with the single-layer ARCs with an average of 5.2% from 0 to 60° over the silicon absorption band. The differences between the ARC-LT simulation and experimental results (see summary in Table I) are caused mainly by the estimation of the deposited ARC thicknesses, refractive index of the ARC layers, and geometrical fluctuations of the nanostructured light trapping pattern over large area.

III. CONCLUSIONS

In this work, we have demonstrated the optimization of a broadband, angle-independent antireflection coating for use on light trapping nanostructured solar cells. The reflectivity performance of single-layer and bilayer antireflection coatings on patterned and bare silicon substrate are numerically simulated and experimentally verified for both conformal and nonconformal scenarios as conventional film deposition systems, such as PECVD and ALD, do not produce conformally coated films. Numerical simulations show that lower step coverage of a deposited film results in a lower wavelength-integrated reflectance. The wavelength-integrated simulated reflectance from optimized nonconformal single-layer SiO_2, Si_3N_4, and Al_2O_3 is shown to be 3, 2.2, and 2.3%, respectively, whereas a minimum of 1.5% is achieved from a Si_3N_4-SiO_2 bilayer ARC, at normal angle of incidence. The optimized bilayer ARC is significantly independent of the angle of incident with angle-averaged wavelength-integrated reflectance of 1.8 and 5.2% demonstrated numerically and experimentally, respectively, making it a promising candidate for practical ARC-coated nanostructured light trapping solar cells.

TABLE I. Angle-integrated reflectance for single and bilayer ARC on LT silicon substrate.

	Angle-integrated reflectance (%)		
	SiO_2	Si_3N_4	SiO_2-Si_3N_4
Simulations	5.15	3.74	1.75
Experiment	7.02	5.76	5.17

IV. METHODS

A. Light trapping nanostructure fabrication

The LT architecture comprises a hexagonal array of post. The optimized geometry is 500-nm period, 300-nm post diameter, and 140-nm post height. In this work, we used MacEtch technique to develop the top diffractive hexagonal post array. The fabrication starts with the soft nanoimprint lithography by spin coating ~500 nm of diluted SU8 2000.5, followed

by 1-min soft baking at 90 °C. Imprinting is done using a PDMS phase stamp. Oxygen plasma opens up the depressed region in order to have a clear semiconductor interface that is critical in MacEtch process. Next, 35 nm of Au, or any other noble metal (e.g., Au, Ag, Pt), is evaporated through electron-beam evaporation (although sputtering could also be utilized). The film thickness of 30–50 nm results in no sidewall characteristics [49]. A mixture of hydrogen peroxide, hydrofluoric acid (HF), and water (H_2O_2:HF:H_2O) with a ratio of 40:10:1 mL is then used to etch the silicon through the gold interface. At this step, the oxidant injects holes at the metal-semiconductor interface which leads to the oxidation of the semiconductor. The oxidized portion is then etched by the HF solution causing the thin metal to effectively "sink" into the semiconductor. There are a number of parameters that impact the etch rate and porosity such as silicon resistivity, ratio of the HF to the H_2O_2, metal thickness, temperature, etch time, etc [50]. The above process is carried out at room temperature. The gold and SU8 is then removed in gold etchant and piranha, respectively.

B. Antireflection coating deposition

ARC deposition is done by using an atomic layer deposition system (Savannah, Ultratech/CNT) for aluminum oxide at 200 °C with 0.04-s water and 0.1 Trimethylaluminum pulse time, 80-sccm carrier gas flow, and 200-mTorr pressure. Silicon nitride depositions is done by using a PECVD system (Plasma-Therm 790) at 300 °C. 2% silane gas diluted in nitrogen (N_2) is used with the following gas flows: 120-sccm SiH_4, 4.56-sccm NH_3, 400-sccm N_2, 900-mTorr pressure, 20-W rf power with deposition rate of 8–10 nm/min. Silicon oxide is also deposited using the same system at the same temperature with 200-sccm SiH_4, 412-sccm N_2O, 1050-mTorr pressure, 25-W rf power and deposition rate of 48–50 nm/min.

C. Optical characterization

Normal-angle reflectance spectra are measured using a microscope-coupled Fourier transform infrared spectrometer system (Hyperion1000-Vertex 80, Bruker Inc.) configured with a CaF_2 UV-vis-NIR beam splitter, silicon diode detector and 4x objective with 0.07 numerical aperture. An aluminum mirror is used as the background reference. Angle dependent reflectance spectra are collected using an integrating sphere (RTC-060-SF, LabSphere Inc.), an UV-Vis-near-infrared spectrometer (HR2000+, Ocean Optics Inc.) and connected with an optical fiber. Unpolarized light was used and the angle scan was from 5 to 65° in increments of 5°.

D. Optical modeling

Reflection spectra are numerically calculated with the FDTD software package (Lumerical Solutions Inc.) based on the experimental parameters for the imprinted 2D grating structure and the ARC layers. Experimental refractive index dispersion of silicon [51] and constant refractive indices of SiO_2 ($n_{SiO} = 1.47$), Si_3N_4 ($n_{SiN} = 2$), and Al_2O_3 ($n_{AlO} = 1.67$) are used. A plane wave is launched at normal incidence and reflectance spectra are captured. For angular simulations the broadband fixed-angle source technique from Lumerical FDTD is used. Both s- and p polarizations are simulated and their average emulates the unpolarized response at non-normal angle of incidence.

ACKNOWLEDGMENT

This work at University of Central Florida was supported by the National Science Foundation under Grant No. ENG/CMMI-1450806.

A.V.-G. and J.B. contributed equally to this work.

[1] X. Yan, D. J. Poxson, J. Cho, R. E. Welser, A. K. Sood, J. K. Kim, and E. F. Schubert, Adv. Funct. Mater. **23**, 583 (2013).

[2] V. M. Aroutiounian, K. Martirosyan, and P. Soukiassian, J. Phys. D: Appl. Phys. **39**, 1623 (2006).

[3] U. Gangopadhyay, K. Kim, D. Mangalaraj, and J. Yi, Appl. Surf. Sci. **230**, 364 (2004).

[4] L. Dobrzański, M. Szindler, and A. Drygała, Open Phys. **12**, 666 (2014).

[5] J. Y. Y. Loh, D. P. Puzzo, P. G. O'Brien, G. A. Ozin, and N. P. Kherani, RSC Adv. **4**, 31188 (2014).

[6] H. Nagel, A. G. Aberle, and R. Hezel, Prog. Photovoltaics **7**, 245 (1999).

[7] J. Schmidt, M. Kerr, and A. Cuevas, Semicond. Sci. Technol. **16**, 164 (2001).

[8] J. Proust, A.-L. Fehrembach, F. Bedu, I. Ozerov, and N. Bonod, Sci. Rep. **6**, 24947 (2016).

[9] K. V. Baryshnikova, M. I. Petrov, V. E. Babicheva, and P. A. Belov, Sci. Rep. **6**, 22136 (2016).

[10] Y. Yao, E. Brueckner, L. Li, and R. Nuzzo, Energy Environ. Sci. **6**, 3071 (2013).

[11] H. K. Raut, V. A. Ganesh, A. S. Nair, and S. Ramakrishna, Energy Environ. Sci. **4**, 3779 (2011).

[12] K. X. Wang, Z. Yu, V. Liu, Y. Cui, and S. Fan, Nano Lett. **12**, 1616 (2012).

[13] S. Zhong, Y. Zeng, Z. Huang, and W. Shen, Sci. Rep. **5**, 8915 (2015).

[14] P. Spinelli, M. A. Verschuuren, and A. Polman, Nat. Commun. **3**, 692 (2012).

[15] Y.-J. Lee, D. S. Ruby, D. W. Peters, B. B. McKenzie, and J. W. P. Hsu, Nano Lett. **8**, 1501 (2008).

[16] J. Zhu, Z. Yu, G. F. Burkhard, C.-M. Hsu, S. T. Connor, Y. Xu, Q. Wang, M. McGehee, S. Fan, and Y. Cui, Nano Lett. **9**, 279 (2009).

[17] P. Kuang, S. Eyderman, M.-L. Hsieh, A. Post, S. John, and S.-Y. Lin, ACS Nano **10**, 6116 (2016).

[18] Y. M. Song, J. S. Yu, and Y. T. Lee, Opt. Lett. **35**, 276 (2010).

[19] S. A. Boden and D. M. Bagnall, Prog. Photovoltaics **18**, 195 (2010).

[20] D. M. Callahan, J. N. Munday, and H. A. Atwater, Nano Lett. **12**, 214 (2012).

[21] T. K. Chong, J. Wilson, S. Mokkapati, and K. R. Catchpole, J. Opt. **14**, 024012 (2012).
[22] A. Mavrokefalos, S. E. Han, S. Yerci, M. S. Branham, and G. Chen, Nano Lett. **12**, 2792 (2012).
[23] J. Kim, E. Lee, M. Ju, H. Kim, J. Yi, S.-J. Moon, M. S. Hyun, and D.-W. Kim, Opt. Express **21**, A607 (2013).
[24] K. J. Yu, L. Gao, J. S. Park, Y. R. Lee, C. J. Corcoran, R. G. Nuzzo, D. Chanda, and J. A. Rogers, Adv. Energy Mater. **3**, 1401 (2013).
[25] S.-M. Lee, R. Biswas, W. Li, D. Kang, L. Chan, and J. Yoon, ACS Nano **8**, 10507 (2014).
[26] G. Li, H. Li, J. Y. L. Ho, M. Wong, and H. S. Kwok, Nano Lett. **14**, 2563 (2014).
[27] I. Karakasoglu, K. X. Wang, and S. Fan, ACS Photonics **2**, 883 (2015).
[28] L. A. Weinstein, W. C. Hsu, S. Yerci, and S. V. Boriskina, J. Opt. **17**, 055901 (2015).
[29] M. S. Branham, W.-C. Hsu, S. Yerci, J. Loomis, S. V. Boriskina, B. R. Hoard, S. E. Han, and G. Chen, Adv. Mater. **27**, 2182 (2015).
[30] D. Shir, J. Yoon, D. Chanda, J.-H. Ryu, and J. A. Rogers, Nano Lett. **10**, 3041 (2010).
[31] J. Boroumand, S. Das, A. Vázquez-Guardado, D. Franklin, and D. Chanda, Sci. Rep. **6**, 31013 (2016).
[32] E. Garnett and P. Yang, Nano Lett. **10**, 1082 (2010).
[33] D. Zhou and R. Biswas, J. Appl. Phys. **103**, 093102 (2008).
[34] R. Dewan and D. Knipp, J. Appl. Phys. **106**, 074901 (2009).
[35] P. Spinelli and A. Polman, IEEE J. Photovoltaics **4**, 554 (2014).
[36] X. Liu, P. R. Coxon, M. Peters, B. Hoex, J. M. Cole, and D. J. Fray, Energy Environ. Sci. **7**, 3223 (2014).
[37] H. Savin, P. Repo, G. von Gastrow, P. Ortega, E. Calle, M. Garín, and R. Alcubilla, Nat. Nanotechnol. **10**, 624 (2015).
[38] A. Barnett, C. Chen, C. Honsberg, D. W. Prather, J. G. Mutitu, S. Shi, and T. Creazzo, Opt. Express **16**, 15238 (2008).
[39] A. Bielawny, J. Üpping, P. T. Miclea, R. B. Wehrspohn, C. Rockstuhl, F. Lederer, M. Peters, L. Steidl, R. Zentel, S. M. Lee, M. Knez, A. Lambertz, and R. Carius, Phys. Status Solidi, A **205**, 2796 (2008).
[40] H.-Y. Chen, H.-L. Lu, Q.-H. Ren, Y. Zhang, X.-F. Yang, S.-J. Ding, and D. W. Zhang, Nanoscale **7**, 15142 (2015).
[41] Y.-J. Peng, H.-X. Huang, and H. Xie, Sol. Energy Mater. Sol. Cells **171**, 98 (2017).
[42] P. K. Singh, R. Kumar, M. Lal, S. N. Singh, and B. K. Das, Sol. Energy Mater. Sol. Cells **70**, 103 (2001).
[43] Y. Jiang, X. Zhang, F. Wang, and Y. Zhao, RSC Adv. **5**, 69629 (2015).
[44] J. Oh, H.-C. Yuan, and H. M. Branz, Nat. Nanotechnol. **7**, 743 (2012).
[45] J. C. Shin, D. Chanda, W. Chern, K. J. Yu, J. A. Rogers, and X. Li, IEEE J. Photovoltaics **2**, 129 (2012).
[46] K. Balasundaram, J. S. Sadhu, J. C. Shin, B. Azeredo, D. Chanda, M. Malik, K. Hsu, J. A. Rogers, P. Ferreira, S. Sinha, and X. Li, Nanotechnology **23**, 305304 (2012).
[47] G. Hass and R. E. Thun, *Physics of Thin Films* (Academic, New York, 1964).
[48] R. E. Sah, *Silicon Nitride, Silicon Dioxide, and Emerging Dielectrics 11* (The Electrochemical Society, Pennington, NJ, 2011).
[49] H.-D. Um, N. Kim, K. Lee, I. Hwang, J. Hoon Seo, Y. J. Yu, P. Duane, M. Wober, and K. Seo, Sci. Rep. **5**, 11277 (2015).
[50] Z. Huang, N. Geyer, P. Werner, J. de Boor, and U. Gösele, Adv. Mater. **23**, 285 (2011).
[51] E. D. Palik, *Handbook of Optical Constants of Solids* (Academic, New York, 1985).